Cell Biomaterials

Article

# On-scalp printing of personalized electroencephalography e-tattoos

## Graphical abstract

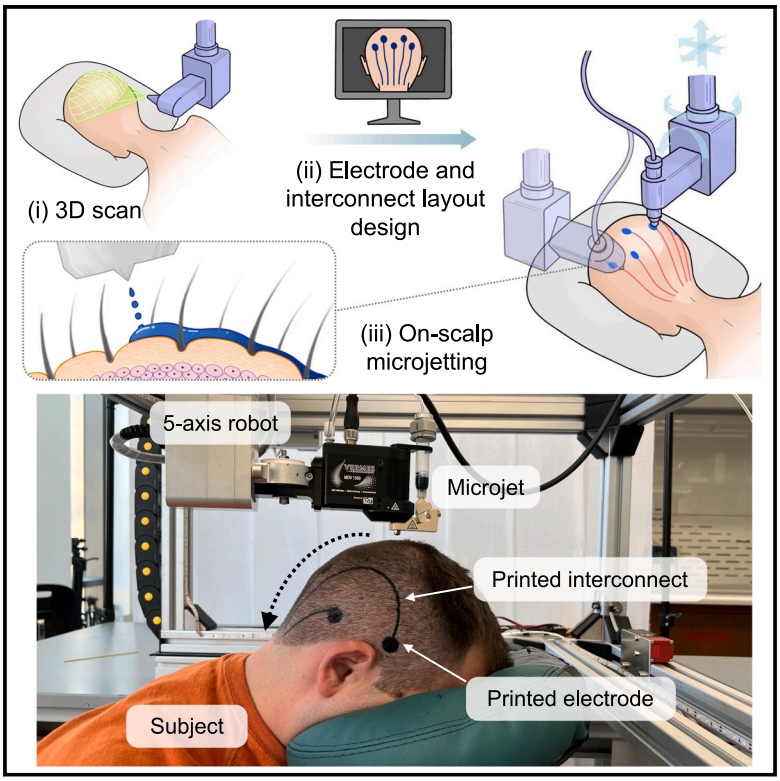


## Highlights

- On-scalp-printed EEG e-tattoos offer personalized, hair-compatible brain monitoring
- Microjet printing safely, precisely, and efficiently delivers custom sensor layouts
- Electrode and interconnect inks are separately designed for sensing and conducting
- Self-drying, skin-conformable e-tattoos enable long-term, high-fidelity EEG

## Authors

Luize Scalco de Vasconcelos, Yichen Yan, Pukar Maharjan, ..., José del R. Millán, Ximin He, Nanshu Lu

## Correspondence

jose.millan@austin.utexas.edu (J.d.R.M.), ximinhe@ucla.edu (X.H.), nanshulu@utexas.edu (N.L.)

## In brief

This study introduces a breakthrough in noninvasive brain-monitoring technology through on-scalp-printed and self-drying conductive inks for electroencephalography (EEG). These ultrathin, skin-conformable temporary e-tattoos provide a comfortable and precise way to capture brain activity, overcoming the limitations of traditional EEG systems, such as bulky equipment and manual setup. With personalized sensor layouts, distinct electrode and interconnect inks, and a hair-compatible digital printing process, these on-scalp-formed e-tattoos represent a promising tool for clinical diagnostics, brain-computer interfaces, and wearable health applications.

Scalco de Vasconcelos et al., 2025, Cell Biomaterials *1*, 100004
January 14, 2025 
https://doi.org/10.1016/j.celbio.2024.100004

CellPress

Cell Biomaterials

CellPress

Article

# On-scalp printing of personalized electroencephalography e-tattoos

Luize Scalco de Vasconcelos,[1,9] Yichen Yan,[2,9] Pukar Maharjan,[1,8] Satyam Kumar,[3] Minsu Zhang,[3] Bowen Yao,[2] Hongbian Li,[1] Sidi Duan,[2] Eric Li,[1] Eric Williams,[1] Sandhya Tiku,[1] Pablo Vidal,[1] R. Sergio Solorzano-Vargas,[4] Wen Hong,[2] Yingjie Du,[2] Zixiao Liu,[2] Fumiaki Iwane,[3] Charles Block,[1] Andrew T. Repetski,[1] Philip Tan,[1] Pulin Wang,[1] Martín G. Martín,[4] José del R. Millán,[3,5,6,*] Ximin He,[2,*] and Nanshu Lu[1,3,6,7,8,10,*]

[1]Department of Aerospace Engineering and Engineering Mechanics, The University of Texas at Austin, Austin, TX 78712, USA
[2]Department of Materials Science and Engineering, University of California, Los Angeles, Los Angeles, CA 90095, USA
[3]Chandra Family Department of Electrical and Computer Engineering, The University of Texas at Austin, Austin, TX 78712, USA
[4]David Geffen School of Medicine, University of California, Los Angeles, Los Angeles, CA 90095, USA
[5]Department of Neurology, The University of Texas at Austin, Austin, TX 78712, USA
[6]Department of Biomedical Engineering, The University of Texas at Austin, Austin, TX 78712, USA
[7]Department of Mechanical Engineering, The University of Texas at Austin, Austin, TX 78712, USA
[8]Texas Materials Institute, The University of Texas at Austin, Austin, TX 78712, USA
[9]These authors contributed equally
[10]Lead contact
*Correspondence: jose.millan@austin.utexas.edu (J.d.R.M.), ximinhe@ucla.edu (X.H.), nanshulu@utexas.edu (N.L.)
https://doi.org/10.1016/j.celbio.2024.100004

**THE BIGGER PICTURE** On-scalp digital printing of custom-designed, temporary-tattoo-like sensors represents a groundbreaking advancement in noninvasive brain-monitoring technologies, advancing the fields of neuroscience, clinical diagnostics, and brain-computer interfaces (BCIs). Traditional electroencephalography (EEG) systems involve time-consuming manual electrode placement, conductive liquid gels, and cumbersome cables, which are prone to signal degradation and discomfort during prolonged use. Our approach overcomes these limitations by combining material innovations with non-contact, on-body digital printing techniques to fabricate e-tattoos that are self-drying, ultrathin, and compatible with hairy scalps. These skin-conformal EEG e-tattoo sensors enable comfortable, long-term, high-quality brain activity monitoring without the discomfort associated with traditional EEG systems. Using individual 3D head scans, custom sensor layout design, and a 5-axis microjet printing robot, we have created EEG e-tattoos with precise, tailored placement over the entire scalp. The inks for electrodes and interconnects have slightly different compositions to achieve low skin contact impedance and high bulk conductivity, respectively. After printing and self-drying, the inks form conductive, stretchable, and breathable thin films that ensure high signal fidelity, even over extended periods. This technology paves the way for non-invasive, high-performance, and user-friendly brain monitoring that will enhance both patient care and the understanding of the human brain. The broader significance of this technology lies in its potential applications beyond traditional EEG use. On-scalp printed ultrathin e-tattoos could play a pivotal role in developing BCIs for various industries, including prosthetics, virtual reality (VR), and human-robot teaming. This work also opens the possibility of on-body digital manufacture of other types of e-tattoo devices in areas beyond the head, leading to large-area, skin-covered yet deformable and breathable functional e-tattoos.

## SUMMARY

Electroencephalography (EEG) is crucial for diagnosing neurological disorders and facilitating brain-computer interfaces. Traditional EEG setups with wet gels and cumbersome cables are labor intensive, uncomfortable, and degrade over time. Dry, skin-conformable e-tattoos offer a comfortable and user-friendly alternative but struggle with hairy scalps. To tackle this problem, we introduce non-contact digital printing of e-tattoos directly on the hairy scalp. Biocompatible inks are crafted for low-impedance electrodes and high-conductivity interconnects. The fabrication system includes a custom sensor layout design algorithm based on individual head scans and a 5-axis robot controlling a microjet printhead for safe and precise

on-scalp ink delivery. After printing, these inks rapidly self-dry into conductive films perfectly conformed to scalp skin, with enhanced wearability, longevity, and skin adhesion compared with gel electrodes and transferred e-tattoos. Motion imagery and error-related potentials are effectively measured by these printed e-tattoos. This innovation heralds a new era in on-body manufacturing of personalized e-tattoos.

## INTRODUCTION

Electroencephalography (EEG) is a non-invasive method that records electrical activity of the brain through sensors placed on the scalp. It has long been a diagnostic tool for conditions such as epilepsy, sleep disorders, and brain injuries as well as a popular sensing modality in neuroscience research.[1,2] Its importance has grown rapidly in recent years with the expansion of brain-computer interfaces (BCI).[3] The international 10–20 system is a widely adopted standard for electrode placement in EEG exams.[4] The "10–20" refers to the distances between the adjacent electrodes being 10% or 20% of the total distance of the skull, adjusted for individual head size. The variation of individual head shapes makes EEG caps with pre-designed openings inaccurate for electrode positioning. Therefore, in clinical settings, a well-trained EEG technician is required to manually mark electrode positions on the patient's head with a ruler and pencil, followed by gel application and cable attachment channel by channel. This laborious process is both costly and time-consuming (1∼2 h)[5] and is also susceptible to human error.[6,7] Furthermore, traditional EEG setups, with their wet-gel electrodes and dangling cables, not only pose risks of detachment and signal interference but also restrict patient mobility.[8] Over time, the gel dries and loses conductivity, limiting the measurements to less than 2 h. For long-term EEG, adhesive pastes or collodion glue are used instead but require periodic maintenance.[9,10] The discomfort caused by the cumbersome hardware can also limit patient compliance, particularly in ambulatory settings or during extended monitoring periods (see details in Note S1).

E-tattoos or epidermal electronics are ultrathin, ultrasoft, skin-conformable electronics that can perform non-invasive biometric sensing on the surface of human skin.[11,12] Traditionally, these devices are pre-fabricated on a handling substrate and subsequently transferred to the skin. However, this method struggles with hairy or highly curvilinear surfaces.[13–16] Moreover, because most biosignals are spatially distributed,[17–20] large-area sensor arrays require personalized design and accurate placement of the sensing channels to accommodate diverse user anatomy and reduce motion artifacts.[21] Although remedies for isolated issues have been reported,[22–26] a universal solution has remained unavailable.

To overcome the aforementioned challenges, we introduce digital printing of custom-designed EEG e-tattoos directly onto the hairy scalp. This approach omits the need for costly e-tattoo manufacture, tedious and inconsistent manual installation of EEG sensors, and bundles of long dangling wires (Figure 1A). It precisely places the electrodes according to the individual user's head shape. We developed printable biocompatible inks based on poly(3,4-ethylenedioxythiophene):poly(styrene sulfonate) (PEDOT:PSS), a highly promising conductive polymer material for bio-interfacing.[27–30] These low-viscosity inks are jetted through the hairs, lightly moistening the scalp before quickly self-drying into soft (Young's modulus 66 < MPa), stretchable (elongation >30%), and conductive thin films (∼ 30 μm thick) that conform perfectly to the skin microtopology without causing mechanical perception. We have formulated two distinct types of inks: one to form electrodes with low skin contact impedance to pick up the faint EEG signals from the brain and the other to form interconnects with high conductivity and high contact impedance to minimize noise pickup.

On-tissue printing is an emerging technology. Previous efforts have primarily focused on bioprinting cell-embedded hydrogels for tissue regeneration[31–33] or strain sensors,[34–36] both in very localized hairless anatomy without requiring specific ink-tissue interfacial electrical properties. Our technique is the first to produce ultrathin e-tattoos directly on human skin for electrophysiology data acquisition despite hairs. Our approach departs from previous on-tissue fabrication technologies in three major aspects (Table S1). First, personalized sensor layout design and printing over large-area, 3D-curvilinear body surfaces are automated through the combination of 3D anatomy scanning, "project-and-slice" 3D surface sensor layout design, and 5-axis robotic control (Figures 1B, 1C, and S1; Video S1). Second, non-contact, fast-speed microjet printing (Note S2; Video S2) instead of extrusion is adopted for high-speed ink droplets to reliably wet hairy skin with uniformity and continuity (Figures S2 and S3; Videos S3 and S4). Lastly, microjet-compatible PEDOT:PSS-based inks are formulated separately for ultrathin electrodes and interconnects (Figure 1D). The printed inks can fully solidify on human skin after 12 min at room temperature without any treatment (Figure 1E), rendering perfectly skin-conformed e-tattoos (Figures 1F, S4, and S5) with much higher adhesion to the skin than transferred e-tattoos (Figures 1G–1J).

## RESULTS

The requirements for the inks are microjet compatibility, biocompatibility, suitable electrical and mechanical properties, and easy removal. These requirements rule out widely used ink curing methods, including UV- or thermo-induced free-radical curing; thermo-, mechanical-, or laser-sintering; or involvement of harsh chemicals. Instead, we opt for spontaneous film formation through water evaporation, as demonstrated in previous works with silver particle dispersion.[31,37–40] For user comfort and mechanical stability, the printed electrodes and interconnects should have a higher stretchability than that of human scalp skin (∼20%),[41] sufficient bending compliance,[14] good skin adhesion, good breathability, stability against sweat and oxidation, and resistance to abrasion.[42] Meanwhile, printed electrodes must have low contact impedance with the skin (40 < kΩ)[43] to achieve high noise rejection (Notes S3 and S4), which is crucial because EEG signals have an inherently low amplitude of 1–100 μV.[2] By contrast,

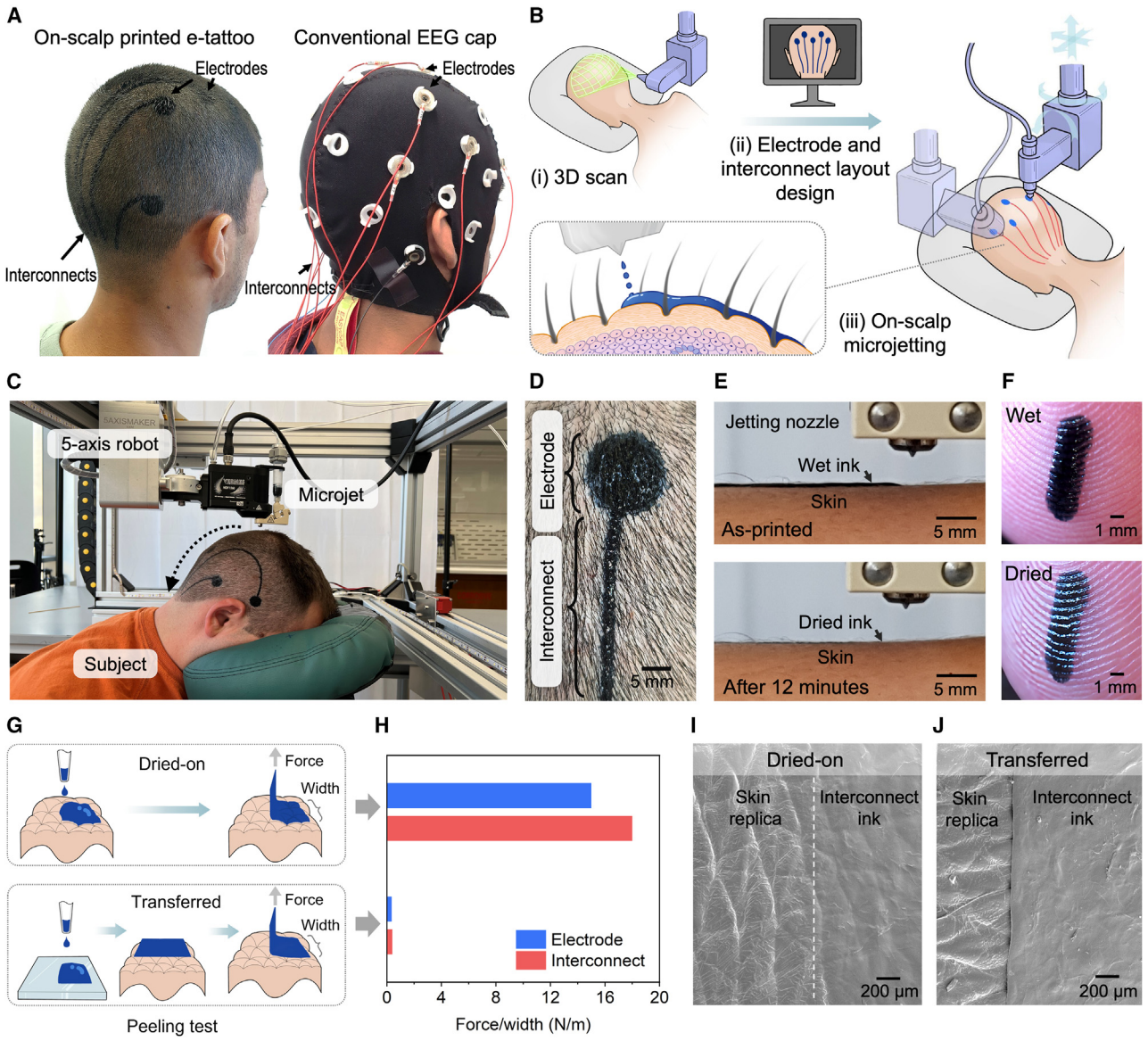


**Figure 1. Overview of the on-scalp EEG e-tattoo printing technology**

Figure360▷ For a Figure360 author presentation of this figure, see https://doi.org/10.1016/j.celbio.2024.100004.

(A) On-scalp printed e-tattoo (left) vs. conventional EEG cap (right).

(B) Schematic illustration of the three main steps of on-scalp e-tattoo printing: (i) 3D head scanning, (ii) personalized electrode and interconnect layout design, and (iii) on-scalp hair-compatible microjet printing.

(C) A photo of the printer setup in which a 5-axis robot controls a microjet printhead for non-contact ink dispensing.

(D) Close-up top view of an electrode and its interconnect directly printed on a hairy scalp.

(E) Close-up side view of the microjetting process on a forearm: as-jetted wet ink layer (top) and solidified thin film after 12 min (bottom).

(F) Top view of the wet ink (top) and dried ink (bottom) on a human fingertip. The solidified e-tattoo can fully conform to the fingerprints.

(G and H) Peeling tests on pig skin show that e-tattoos printed and dried on the skin exhibit much stronger adhesion than those printed on a glass substrate and subsequently transferred to the skin.

(I and J) SEM images of the e-tattoos printed on and transferred to human skin replicas. The printed e-tattoo has much better skin conformability than the transferred e-tattoo. See also Figures S1–S5 and Table S1.

printed interconnects need high skin contact impedance to avoid picking up EEG signals along the way. In addition, a low total interconnect resistance is critical for rejecting electromagnetic interference (EMI) and capacitive noise. As a result, the excessive length of the printed interconnects (up to 50 cm) has to be offset by a sufficiently high bulk conductivity (> 40 S/cm, Note S5). Therefore, two types of inks with contrasting properties need to be formed.

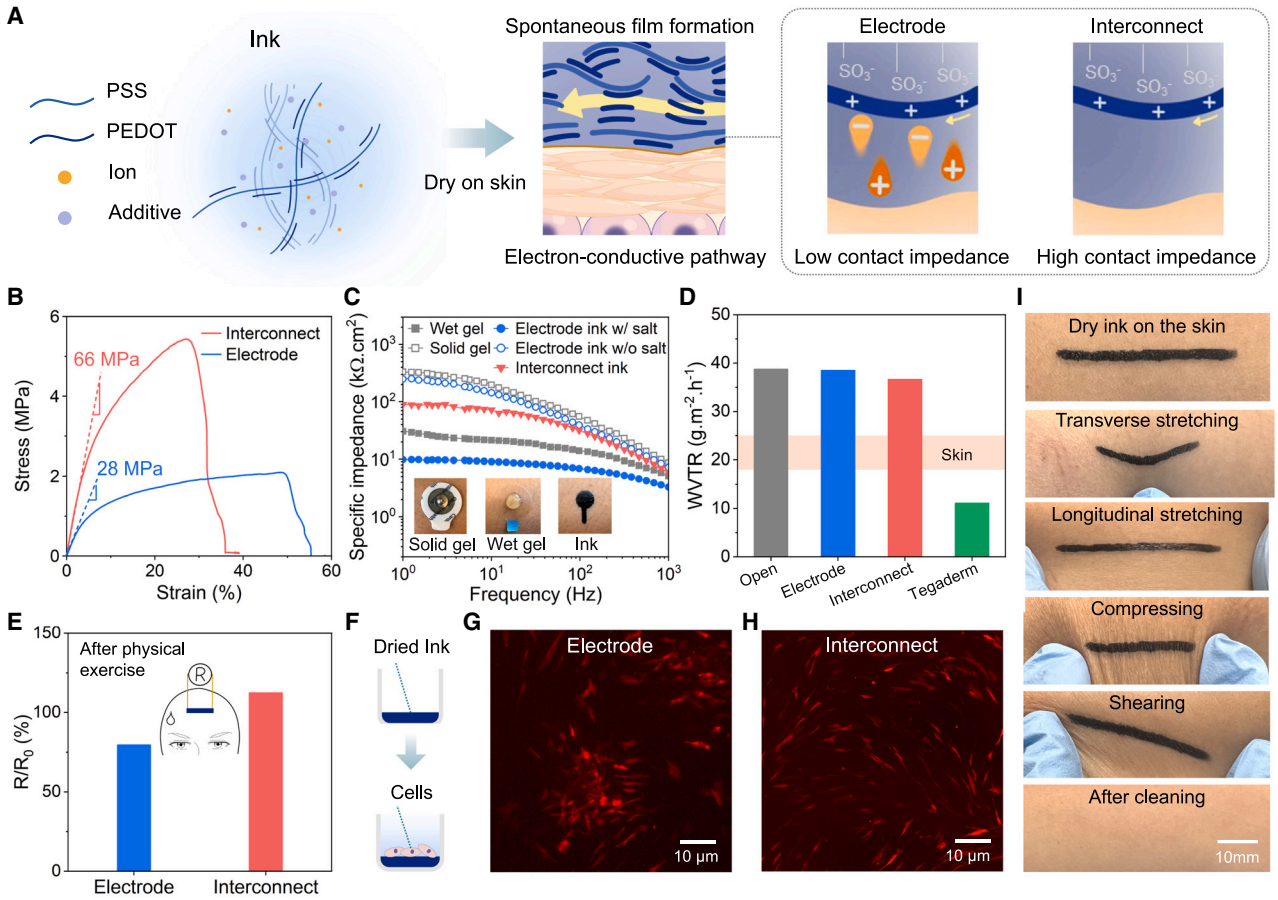


**Figure 2. Properties of the on-skin-printed electrodes and interconnects**

(A) Schematics of the two ink compositions tuned for distinct properties. During the ink-drying process, PEDOT will stack to form electron-conductive pathways (yellow arrow). For electrodes, ink containing NaCl promotes the low contact impedance with the skin needed for EEG acquisition. For interconnects, ink without NaCl demonstrates significantly higher contact impedance when applied to the skin, inherently inhibiting the pickup of EEG signals, whereas the addition of DMSO enhances the bulk electron conductivity required due to lengthy routing.

(B) Stress-strain curves of the dried electrode and the interconnect films show stretchability over 30%.

(C) Comparison of the specific contact impedance of different electrode inks with wet and solid commercial gel electrodes. The NaCl-containing ink has the lowest value, 9 kΩ·cm$^2$ at 10 Hz.

(D) Water vapor transmission rates (WVTRs) through the electrode and interconnect films are similar to that of an open vial and higher than that of the human skin.[52,53] By contrast, the 3M Tegaderm tape has a much lower WVTR.

(E) Intense physical exercises did not drastically alter the resistance of the interconnect and electrode traces.

(F) Schematic of cell culturing experiment on dried inks.

(G and H) Fluorescent images of human skin fibroblast cells grown on the electrode and interconnect films for a period of 3 days reveal favorable fiber morphologies, suggesting that both inks exhibit good biocompatibility.

(I) Photos showing that the interconnect film formed on the skin can withstand large mechanical deformations, indicating good robustness and adhesion. The interconnect can be easily removed by wiping with an alcohol wipe or soapy water, leaving no residue or discoloration on the skin. See also Figures S6–S17 and Table S2.

To meet all the aforementioned criteria using a novel approach, PEDOT:PSS (Figure 2A) was selected as the principal material for both electrode and interconnect inks because of its ability to disperse in water, form films upon drying, and its recognized biocompatibility.[44–46] Glycerol and dimethyl sulfoxide (DMSO) are also biocompatible, having been used in skincare products and as cryoprotectants in the cryopreservation of cells and biologics.[47] They were added to the interconnect ink to strike a balance between mechanical compliance and electrical conductivity. DMSO enhances both conductivity[45,48] and stretchability, but its influence maxes out at ~10% strain before breaking (Table S2). Hence, the plasticizing ability of glycerol[49,50] was used to further lower the elastic modulus to 66 MPa and enhance the stretchability to 30% (Figure 2B). Furthermore, the secondary doping effect of glycerol benefits the electrical properties,[51] resulting in a sufficiently high conductivity of 83 S/cm. Ultimately, the interconnect made from PEDOT:PSS, DMSO, and glycerol showed sufficient and stable conductivity on the skin for over 24 h of wear (Figure S6). The resistance of the free-standing interconnect thin film remained almost constant

under 100 cycles of repetitive strains between 0% and 10% (Figure S7).

For the electrode ink, sodium chloride (NaCl) was introduced to increase ionic conductivity and thus promote low contact impedance with the skin because ions can cross the stratum corneum through existing appendageal pathways.[54] Although the NaCl-free interconnect exhibited high skin contact impedance (72 kΩ. $cm^2$ at 10 Hz) to suppress signal pickup, the NaCl-containing electrode achieved an 8-fold lower contact impedance (9 kΩ. $cm^2$ at 10 Hz), which is much lower than commercial solid-gel electrodes and on par with commercial wet saline gels (Figure 2C). Note that this low contact impedance was achieved without any skin abrasion prior to ink printing (Figure S8; Note S5). The NaCl addition to the electrode ink also reduced the elastic modulus from 130 MPa (Table S2) to 28 MPa (Figure 2B), which can be attributed to the weakening of the Coulombic interactions between PEDOT and PSS.[55] Furthermore, the contact impedance remained below 40 kΩ· $cm^2$ for over 20 h (Figure S9) without causing any skin irritation (Figure S10), indicating its potential for long-term recording.

The tunable viscosity and shear thinning of aqueous PEDOT:PSS solutions enable excellent printability using microjetting (Figure S11; Note S2). The measured contact angles of the electrode and the interconnect inks were 47.54° and 74.52° (Figures S12A and S12B), respectively, which are in the optimal range for jet printing, allowing good adhesion and spreading on the skin while avoiding bleeding to maintain adequate printing resolution.[56] Through a covered vial setup, the water vapor transmission rate (WVTR) of the electrode and interconnect at 21.5°C and 35% humidity was measured to be 38.5 and 36.6 g · $cm^{-2}$· $h^{-1}$, respectively, which are similar to that of the control case without any cover (38.8 g · $cm^{-2}$· $h^{-1}$) (Figures 2D and S13). This high breathability can be attributed to the low thickness (∼30 μm, Figure S14) and water diffusivity of the PEDOT:PSS film.[57] The combined stretchability and breathability of the solidified inks limited the resistance change to less than 25% after heavy exercises (16 10-min jumping jack sessions during 4 h) for both electrode and interconnect traces on the forehead, demonstrating sufficient stability despite sweat (Figures 2E and S15). Human skin fibroblast cells cultured on the dried inks became fiber shaped and showed proliferation over time (Figures 2F–2H) comparable to the control (Figure S16), demonstrating the biocompatibility of the e-tattoos. Furthermore, no skin discoloration was observed after 6 h of electrode or interconnect coverage (Figure S17).

The printed and dried electrode and interconnect can withstand repeated deformation, owing to their low modulus, high stretchability, and good adhesion with skin (Figure 2I; Video S5). However, the inks can be easily removed with soapy water or alcohol wipes (Video S5).

Conventional EEG recordings are typically conducted using elastic caps with pre-arranged openings for gel injection in accordance with the international 10–20 system.[4] However, variations in head shapes can frequently cause suboptimal electrode positioning and insufficient contact between certain regions of the cap and the scalp, resulting in noisy signals or complete loss of signal.[1,58] Such issues can be eliminated by personalized sensor design and cap-free electrode placement (Note S6). First, a 3D scanning app (ScandyPro) on an iPhone 13 mounted on the 5-axis robot revolves around the participant's head to generate an unstructured triangulated surface representation of the head. We then define the electrode coordinates on this scanned head surface using an open-source function in MATLAB called MeshEEG.[59] For generic components with small dimensions, such as the electrodes with a selected diameter of 1.5 cm, it is sufficient to project a 2D template pattern (e.g., zigzag shown in blue in the upper left corner of Figure 3A) onto the target area in the mesh element plane. The straightforward nature of this printing path is facilitated by the robustness of the non-contact microjet printing method (Table S3; Note S2), allowing deposition to proceed unaffected by minor changes in the distance from the nozzle to the skin surface. This is not the case for typical continuous extrusion printing, where any hair obstruction or small changes in the nozzle-to-surface distance can easily disrupt the ink trace. In addition, the low-profile microjet nozzle is safer for on-body printing than the long and sharp needles used in typical extrusion printing.

Given the significant length (ranging from 5∼30 cm for a typical 10–20 montage) required to route the interconnects from the electrodes to the back of the neck where the amplifier is attached, a different approach is adopted to design the layouts of the interconnects. The algorithm identifies the intersections between the meshed scalp and the plane encompassing the electrode, its terminal at the back of the neck, and an intermediate point (e.g., $C_4$, $T_{C4}$, and $I_{C4}$ in Figure 3A), detailed in Note S6 and Figure S18. The overall electrode-interconnect design algorithm is therefore referred to as the project-and-slice algorithm.

After pose matching the digital head model with the physical head position via three fiducial markers on the head, the algorithm converts the electrode-interconnect toolpath into a series of control commands (G-code) for the 5-axis robot (Figures 3B and S19). The algorithm plans the position and orientation of the robotic end effector so that the jetting axis is perpendicular to and at a fixed distance from the target surface. Should there be major head movement during printing, the G-code is regenerated based on the updated coordinates of the fiducials.

To assess the precision of our printing method, we performed a second 3D scan after printing and measured the offset of the central position of the printed electrode compared with its designed location (Figure 3C). The average deviation was ∼4 mm, with a maximum error less than 8 mm (Figure 3D). The error mainly stems from the limited accuracy of the 3D scan of the head shape through an elastic cap (not the electrode cap) used to suppress the hairs and smooth the surface. For medical applications such as epilepsy diagnosis, more precise head models constructed from X-ray tomography or magnetic resonance imaging (MRI), typically used in conjunction with EEG,[60] can be incorporated to further enhance electrode placement accuracy. Furthermore, regression and machine learning techniques may improve the accuracy of head shape prediction despite hair coverage.[61,62]

In a study measuring the channel impedance across 10 locations for each of the five subjects (Figures 4A and S20), the on-scalp printed electrode-interconnect e-tattoos showed a significantly lower average impedance (24.6 ± 22.0 kΩ) than traditional wet saline gel electrodes (53.3 ± 37.8 kΩ), with a notable statistical

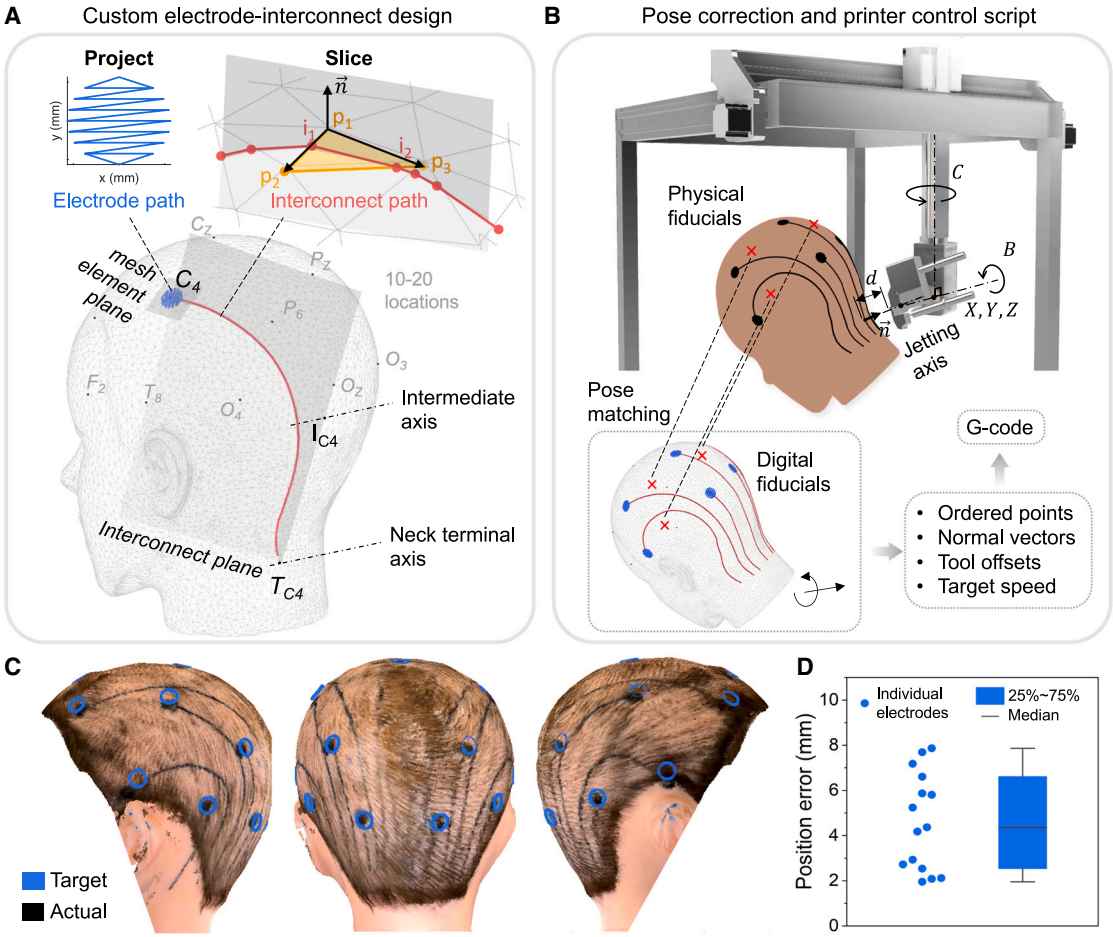


**Figure 3. Method for the personalized design and printing of electrodes and interconnects on human heads in accordance with the international 10–20 system**

(A) Project-and-slice algorithm to generate a custom electrode-interconnect array on a 3D triangular mesh model of the scanned head. The electrode (in blue) is projected from a 2D path template onto the 10–20 locations. The interconnect (in red) is generated by slicing the mesh with a plane encompassing the electrode (e.g., $C_4$), its corresponding terminal ($T_{C4}$), and an intermediate point ($I_{C4}$).

(B) The post-processing algorithm aligns three fiducial points on the digital model with those on the physical head to match the poses and generates control instructions $(X, Y, Z, B, C)$ for head-conformable printing with the jetting axis normal to the scalp ($\vec{n}$) and at a fixed distance ($d$).

(C) Assessment of the printing accuracy on a hairy mannequin. The intended electrode locations (in blue) are overlaid with a 3D scan of the scalp post-printing (black electrode and interconnect traces).

(D) Distance between the printed and intended electrode positions across different EEG channels (circles correspond to individual electrodes, and the boxplot shows statistical metrics). The error bar indicates the minimum and maximum deviations. See also Figures S18 and S19.

difference ($p < 0.0001$). This lower and more uniform impedance across the board is critical for recording high-fidelity EEG data in ambulatory conditions where temperature fluctuations, EMI, and motion-induced changes in skin potentials are not controllable.[43,63,64] The smaller variation in the impedance of the printed electrodes compared with gel electrodes proves that the microjet printing through the hairs and over the curved surface of the head is robust and repeatable. After 6 h, the performance of the gel electrodes deteriorated drastically, with 37% of the channels unmeasurable and most of the remaining ones showing impedance values above 200 kΩ, which is considered unsuitable for EEG (Figure 4B, Note S3). By contrast, the on-scalp printed electrodes and interconnects maintained a stable impedance below 40 kΩ even after 6 h. As expected, the skin-electrode interface dominates the channel impedance, with only a minor contribution from the interconnect trace (stable routing resistance 2 < kΩ for 6 h, Figure S21). To limit EEG recording to the electrode site and inhibit signal pickup along the interconnect, the interconnect ink was designed to provide high contact impedance (Figure S22; Note S4). It was confirmed that no meaningful difference was observed between the EEG recorded using an electrode routed with an interconnect in direct contact with the skin versus an electrode routed with an interconnect printed on top of a thick electrically insulating latex layer (Figure S23). EEG recording during head-turning movements was equivalent between gel and printed electrodes (Figure S24). Both freshly applied gel and printed electrodes

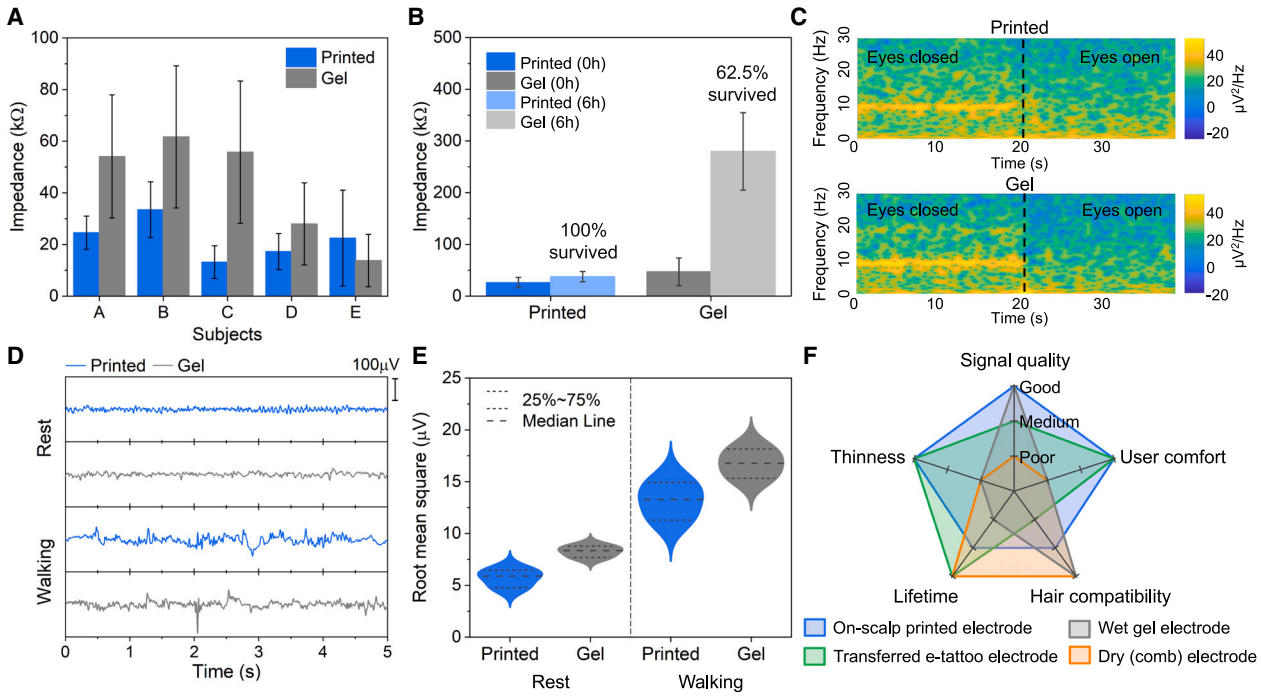


**Figure 4. EEG recording performance of the on-scalp printed electrodes benchmarked against commercial wet-gel electrodes**

(A) Average contact impedance of 10 printed (in blue) and gel (in gray) electrodes on each of the five subjects right after application, i.e., at 0 h. The printed electrodes have low impedance with a narrow distribution across subjects and scalp locations, whereas gel electrodes show higher average impedance with greater variability.

(B) Comparison of the average contact impedance of all subjects at 0 h and after 6 h confirms that gel electrodes are unsuitable for long-term EEG (27.5% are disconnected, and the remainders show exceedingly high impedance, i.e., over 200 k Ω). In comparison, all printed electrodes maintain low impedance after 6 h. Error bars indicate one standard deviation.

(C) EEG spectrograms confirm the presence of the expected alpha wave (10 Hz) with eyes closed for both printed and gel electrodes.

(D and E) EEG waveforms and root mean square values during rest and motion are comparable between printed and gel electrodes.

(F) A comparative evaluation of various types of EEG electrodes (on-scalp printed, transferred e-tattoo, wet gel, and dry comb) across several metrics (signal quality, thinness, electrode lifetime, user comfort, and hair compatibility) shows that on-scalp printing is the only technology without any major drawbacks (rating criteria in Table S4). See also Figures S20–S24.

successfully detected alpha waves when participants closed their eyes (Figure 4C), and both types recorded comparable signals during rest or walking states (Figures 4D and 4E). The advantages of on-scalp printing technology compared with alternatives are evident in a radar chart (Figure 4; rating criteria in Table S4). The on-scalp printed e-tattoo technology merges the hair-friendly and low contact impedance features of wet-gel electrodes with the dry, sleek benefits of e-tattoos, all while being a cost-efficient and time-saving method of digital production.

To assess the stability and effectiveness of the printed electrodes and interconnects in capturing specific EEG signals over time, under institutional review board (IRB) approval, we performed sensor printing and EEG measurements on five different participants, focusing on two popular BCI markers: motor imagery (MI) and error-related potential (ErrP) (Figure 5A). Eight electrodes over the motor cortex and medial line (Figures 5B and S25) recorded each EEG marker under three experimental conditions: with fresh gel electrodes (gel-0 h), freshly printed electrodes (printed-0 h), and printed electrodes after 6 h of wear (printed-6 h). Due to the ineffectiveness of gel electrodes after 6 h (Figure 4A), no EEG could be measured.

We evaluated signal quality in MI-based BCI experiments by analyzing the number of rejected 1-s EEG samples. A single-factor repeated measures analysis of variance (ANOVA) revealed no statistically significant difference among the three conditions ($p$ = 0.2018; printed-0h: 8.53 ± 0.78%, printed-6 h: 15.55 ± 11.83%, gel-0 h: 8.18 ± 0%; Figure 5C). In particular, the group means for fresh gel and freshly printed electrodes were similar, with only ~10% of all acquired samples being rejected. A slightly higher rejection rate was noted in the printed-6 h condition, likely attributed to deteriorated terminal-to-cable connection at the highly deformable back of the neck given the previously confirmed stable electrode-interconnect contact impedance after 6 h.

We also quantified the event-related desynchronization (ERD) over the motor area contralateral to the right hand during the MI task (three channels on the left lobe). All three conditions showed a desynchronization effect (Figure 5D); printed-0 h: − 37.82 ± 16.17%, printed-6 h: − 37.60 ± 10.35%, and gel-0 h: − 35.04 ± 7.19% with no significant differences found ($p$ = 0.8305). Additionally, we observed a stable trend in the ERD captured by the printed electrodes during the two recording

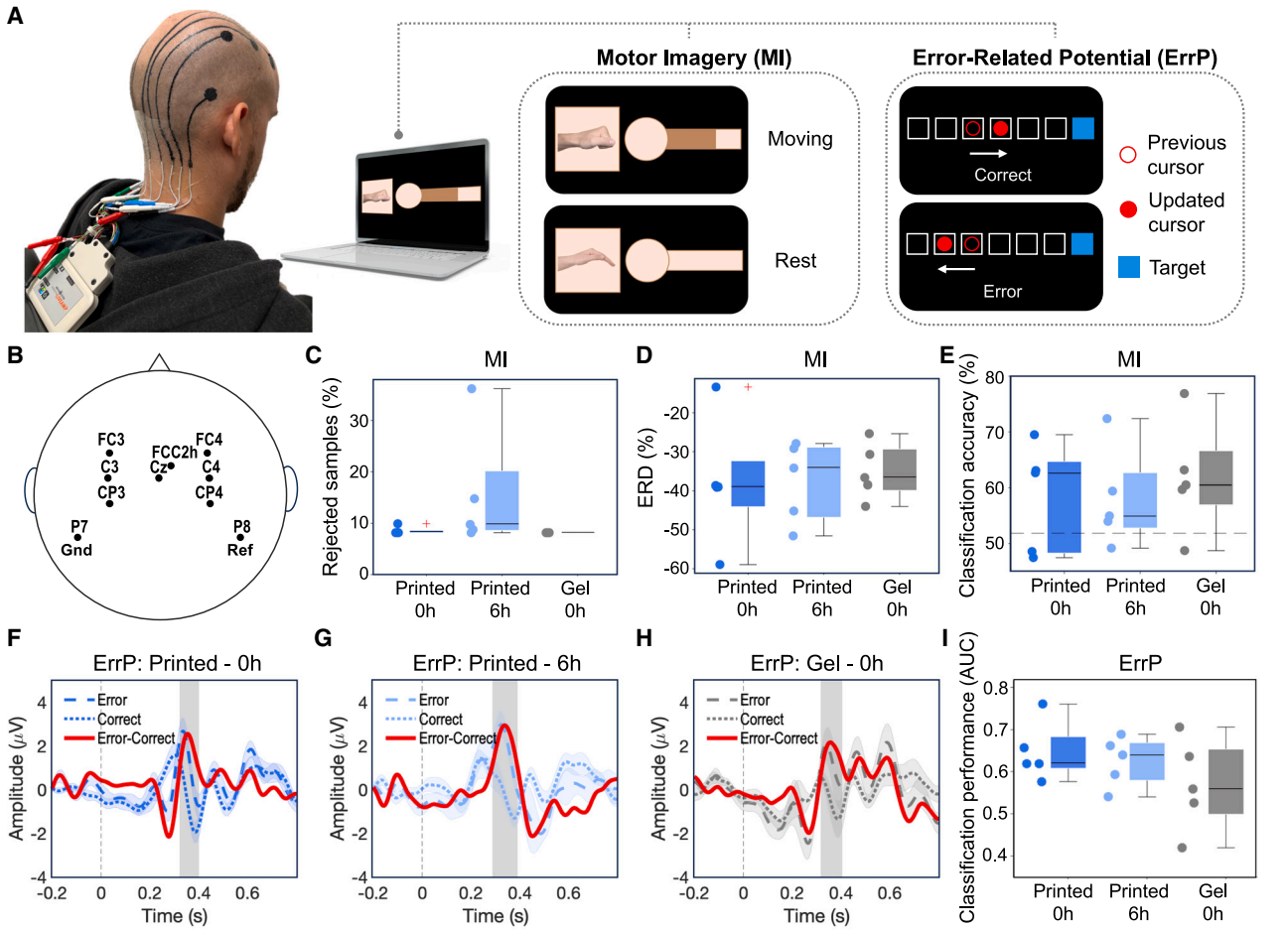


**Figure 5. BCI performance of printed electrodes (immediately and 6 h post-printing) compared with conventional wet-gel electrodes immediately after application because they become unusable after 3∼5 h**

(A) A photo of printed electrodes and interconnects connected to BrainVision amplifier and illustrations of experiments to elicit the two EEG markers: MI and ErrP.

(B) Printed EEG electrode montage.

(C) Fraction of 1-s EEG samples rejected during MI trials.

(D) Event-related desynchronization (ERD) observed in MI trials.

(E) Accuracy of MI classification based on leave-one-run-out cross-validation.

(F–H) Grand-averaged ErrP.

(I) Classification performance of ErrP using leave-one-block-out cross-validation. In the boxplots, the central line indicates the median, the box bottom and top edges indicate the 25th and 75th percentiles, respectively, and the whiskers extend to the maximum and minimum values. See also Figure S25.

sessions. For the performance assessment of the MI-based BCIs, cross-validation analysis was conducted for each condition (Figure 5E). The mean classification accuracy among different participants under all conditions (printed-0h: 58.23 ± 9.74%, printed-6h: 57.97 ± 8.84%, gel-0h: 61.78 ± 10.08%) outperformed chance level (51.83%) with no significant differences among them ($p$ = 0.7849). Although we observed MI performance lower than chance for some subjects under some conditions, the literature has shown that MI-BCI is a user-in-the-loop system and requires longitudinal user training over multiple days to acquire the skills necessary to operate it reliably,[65,66] which was not performed in our protocol.

Figures 5F–5I illustrate the grand-averaged ErrP across all trials of all subjects at the Cz channel with respect to the stimulus onset. ErrPs are characterized by the time-locked components of positivity and negativity relative to cue onset.[67,68] Gray shaded zones denote the time window in which the cluster-based permutation test of the individual block-wise averaged error and correct trials with Benjamini-Hochberg correction resulted in $p$ values below 0.05. Our analysis demonstrates similar significant temporal windows in all three conditions—printed-0h, printed-6h, and gel-0h—where error positivity around 0.4 s was observed. Classification analysis of the ErrP data from individual subjects resulted in the classification performance of the area under the curve of 0.65 ± 0.070, 0.62 ± 0.059, and 0.57 ± 0.11 for each condition, respectively (Figure 5I). No significant differences in classification accuracy were found between the three conditions ($p$ = 0.44).

The analysis across the two EEG markers demonstrates that our printed electrodes perform comparably to standard gel electrodes. Additionally, compared with conventional wet-gel electrodes, the printed electrodes extended the electrode lifetime to at least 6 h and ensured consistent performance over multiple sessions.

## DISCUSSION

On-scalp e-tattoo printing has the potential to drastically shorten the EEG setup time. In our study, 3D head scanning and printing of 10 electrodes can be completed within about 15 min. However, head movements require additional calibration to update the coordinates of the landmarks, adding an extra 5 min per movement. Hence, incorporating visual tracking systems into the printer to create a closed-loop control can enable faster on-scalp manufacturing. Note that although the current on-scalp printing process requires a time commitment of the participant, it is time- and cost-saving compared with the conventional microfabricated e-tattoos in addition to the benefits of personalization, hair compatibility, and large-area coverage. More work is needed to scan and print on heads with long and thick hairs. Highlighting the persistent issue of racial bias in neuroscience research is crucial, as traditional EEG electrodes are often unreliable on individuals of African descent, resulting in suboptimal patient experiences and outcomes in clinical settings.[69,70] Curly hairs tend to push against the EEG cap, reducing contact between the electrodes and the scalp, leading to a poor contact impedance.[71] Developing on-scalp digital printing for different hair types should prioritize bridging this important gap.

E-tattoos must retain their form and functionality when exposed to external factors such as abrasion to be effectively used in applications such as sleep monitoring and to integrate seamlessly with other head-wearable devices, such as virtual reality (VR) headsets and protective helmets.[72] Thus, further enhancing the adhesion between the printed e-tattoos and the scalp skin without complicating its removal is an important future research direction. Other opportunities include on-scalp printing of diverse ink types, such as semiconductors and dielectrics[40,73] for operational amplifiers, enabling active signal amplification similar to existing active EEG electrodes based on rigid electronics.

In a broader sense, the introduced method for on-body digital printing addresses the persistent issue of traditional e-tattoos not being compatible with extensive regions of intricate 3D or hair-covered skin surfaces. Over the years, despite rapid progress in functionalities and wearability, e-tattoos have remained costly to fabricate, small in size, and restricted to relatively flat and glabrous skin surfaces.[13,14,16] Surmounting these limitations will allow for spatial mapping of physiological signals across extensive and curved body surfaces. This advancement is appealing for numerous applications beyond EEG, such as electromyography (EMG) and transcutaneous electrical nerve stimulation (TENS), pertinent to human-machine interfaces, performance training, and rehabilitation. Moreover, it possesses the capability for sensor integration on internal organs, such as on the cranium for electrocorticography (ECoG) recordings,[74] on the heart for electrocardiogram (ECG) monitoring or stimulation,[75] to aid in wound healing,[32] and on tissue or bone for regeneration purposes.[76–78] Ultimately, it opens the door for the on-body integration of sensing, processing, communication, and power components tailored specifically to the anatomy and needs of the user.[79,80]

In summary, we have developed a safe digital printing method that allows for the direct creation of customized, ultrathin, stretchable, and skin-conformal e-tattoos on a hairy scalp. These e-tattoos are electrically conductive and mechanically, as well as physiologically, unnoticeable, offering full-head, high-fidelity, long-term, and comfortable EEG recording capabilities without the need for labor-intensive and short-lived wet-gel electrodes, as well as cumbersome cables and caps. The specialized electrode and interconnect inks allow for microjet printing, self-drying, and high-fidelity EEG recording from specific sites. Additionally, a tailored project-and-slice algorithm streamlines the personalized electrode-interconnect layout design in adherence to international standards. The system has been validated against traditional gel electrodes used with EEG caps. This innovation significantly expands the potential applications of e-tattoos for EEG by solving many long-standing challenges. It marks a new chapter in neurotechnology, emphasizing customization and accuracy, enhancing patient well-being, and minimizing healthcare labor.

## EXPERIMENTAL PROCEDURES

### Ink formulation

Poly(3,4-ethylenedioxythiophene):poly(styrene sulfonate) (PEDOT:PSS) (ICP 1050, 739332, Sigma-Aldrich) was freeze-dried using liquid nitrogen and a Labconco FreeZone 1 Freeze Dryer. To make the electrode ink, 11.6 mg NaCl (S271, Fisher), 60 mg dried PEDOT:PSS, and 60 mg glycerol (AA36646, Fisher) were added to 2 g deionized (DI) water. To make the interconnect ink, 60 mg dried PEDOT:PSS, 60 mg glycerol, and 120 mg DMSO (D128, Fisher) were added to 2 g DI water. A glass rod was used to thoroughly mix the ingredients. A 4°C fridge was used for long-term ink storage.

### Ink characterization

#### *Tensile tests*

The inks were dried in molds made of Ecoflex 00-30 (Smooth-on). Then, the dry films were tested by a dynamic mechanical tester (DMA 850, TA Instruments) under a strain rate of 0.05/min. The film thicknesses, 15∼20 μm, were determined by scanning electron microscopy (SEM). The stiffness at 1% strain was used for modulus calculation.

#### *Conductivity measurements*

The inks were dried in molds made of Ecoflex 00-30 (Smooth-on). Then, the dry films were tested by electrochemical impedance spectroscopy (EIS) mode using a CHI660e electrochemical workstation. The resistance does not change with frequency, indicating the dried inks are electrically rather than ionically conductive. The thicknesses were determined by SEM.

#### *SEM images of films on skin phantom*

First, a reverse mold of the skin was made by pouring Ecoflex 00-30 (Smooth-on) on the forearm of the author and waiting for 30 min for curing. Then, Ecoflex 00-30 was poured on the reverse mold to form the skin phantom. Before making the skin phantom, the reverse mold was treated by chemical vapor deposition using trichloro(1H,1H,2H,2H-perfluorooctyl)silane (448931, Sigma-Aldrich) to ensure the successful detachment of the skin phantom from the reverse mold. The ink was dried on a flat glass substrate, which was then transferred to the skin phantom. For the transfer-on-skin film, the ink was also applied on a separate piece of skin phantom with controlled mass, which will yield a film with the same mass per area as the transferred-on film. The SEM images were taken using a Zeiss Supra 40VP SEM.

### Peeling force tests of the inks on porcine skins

Porcine skins were purchased from a supermarket and were glued on a glass substrate using superglue. Both electrode and interconnect inks were tested for two conditions: (1) the inks were dried on a flat glass substrate and then transferred to the porcine skin, and (2) the inks were deposited directly on porcine skin in controlled amounts to yield a film with the same mass per area as the transferred-on film. The peeling test was done using a UStretch tensile test machine from CellScale. Scotch Super 33+ tape was used as the backing during the peeling test (Figure S26). The data reported in Figure 1F were the average values from the stable peeling region when no tearing happened.

### Ink contact angle measurements

100 μL of ink was placed on various surfaces to form a droplet at room temperature. The figures are taken by camera (FL3-U3-13Y3M-C, Point Gray) with a micro-image lens (Zoom 125, OPTEM) and processed by ImageJ software.

### Ink viscosity measurements

The viscosity was measured by a rheometer (HR30, TA Instruments) equipped with 25 mm parallel plates with a 1-mm gap. The tests were done at room temperature.

### Electrical properties under mechanical strain and stability tests

The interconnect and electrode ink were casted on a 1-mm-thick polydimethylsiloxane (PDMS) substrate through a medical tape mask and dried at room temperature. Then, the mask was removed, and the PEDOT:PSS film with a width of 5 mm and a length of 20 or 10 mm was obtained. The thickness of the sample is 30 μm. Two copper traces with 1 mm in width were attached to the two ends of the PEDOT:PSS film through silver paste. Next, the sample was dried on a hotplate at 90°C for 10 min. After this, the silver paste at the two ends was encapsulated with half-cured PDMS and cured in an oven of 70°C for 30 min. The specimen was fixed on a dynamic mechanical analyzer and stretched at a speed of 0.1 mm/s. The resistance was simultaneously recorded with an inductance-capacitance-resistance (LCR) meter (3532–50 LCR HiTester, Hioki). The repeated stretching was tested under oscillation mode at a strain of 10%, and the oscillation frequency was 0.5 Hz.

### Skin interfacial impedance tests

EIS was used to characterize the skin-electrode interfacial impedance of different electrode materials across the frequency range of 0.1 to 1,000 Hz (Autolab, Metrohm). In addition to our electrode ink, three commercial gels were characterized: saline wet-gel (Signagel, ParkerLabs), non-saline wet-gel (Spectra 360, ParkerLabs), and solid-gel button electrodes (Kendall H124SG 1″, Corvidien). For Note S4, we also test a commercial water-based carbon ink (Electric Paint, Bare Conductive) and a silver ink. The silver ink fabrication followed the procedure in Zhu et al.[31] by first dissolving 2.5 wt % polyethylene oxide (PEO) (Mv 1,000,000, Sigma-Aldrich) in 1:4 water:ethanol solution and then adding silver flakes (10 μm, Sigma-Aldrich) such that the dry ink weight ratio is 9:1 Ag:PEO. The forehead of the subject was first cleaned with a soft alcohol wipe (alcohol prep pads, CareTouch), without any abrasion. A pair of each type of electrode was then applied to the forehead. For the wet-gel and ink electrodes, stickers with a circle cutout in the center (washers, inner diameter 8 mm, BrainVision Solutions Inc) were used to delimit the area and ensure consistent coverage. Standard EIS measurement was carried out, and the measured impedance was normalized by the electrode area.

### Skin conformability mechanical analysis

The mechanical analysis of the printed and transferred e-tattoo skin conformability for both electrode and interconnect inks (Figure S27) was carried out using the energy minimization method by Wang and Lu[81] as detailed in Note S5.

### Sweat stability measurements

Both inks were applied on the forehead of a test subject and let dry. A sweat patch (Figure S15) was affixed to adjacent skin, and an exercise session was conducted to stimulate sweat production. The exercise consists of 10-min sessions of jumping jacks followed by 5-min breaks for 4 h at room temperature, performed by a female researcher. The resistance before and after the exercise was measured by EIS mode using a CHI660e electrochemical workstation.

### Breathability of electrode and interconnect films

The water vapor transmission rate (WVTR) of the electrode and interconnect films was measured based on ASTM E96. Briefly, the ink of the electrode or the interconnect was poured onto an Ecoflex mold and was dried on a hotplate at 50°C for 15 min. After the film was fully dried, it was peeled off from the Ecoflex mold, and a free-standing film of electrode or interconnect with a thickness of ~30 μm was obtained. Then the film was used to seal a glass bottle filled with 0.5 g DI water with a rubber band to fix the film onto the glass bottle. Another glass bottle with DI water but no cover was used as the control sample. Finally, the bottles were put in a chamber with a temperature of 21.5°C and a humidity of around 35%. The samples were weighed at different periods for 7 days to measure the weight change of water. The WVTR was calculated by the water loss using the following formula:

$$WVTR = \frac{\Delta m}{AT} \quad \text{(Equation 1)}$$

where Δ m is the weight loss of water, A is the mouth area of the glass bottle, and T is the time.

### Cell test

Cell preparation: skin fibroblast cells were obtained from a patient (UCLA institutional review board [IRB] number IRB#11-002778) and were propagated and maintained in the DMEM-F12 media (Dulbecco's Modified Eagle Medium, 11965092, Gibco) supplemented with 10% fetal bovine serum (FBS, 26140079, Gibco) and 1% Anti-Anti (antibiotic-antimycotic, 15240-062, Gibco). TrypLE (TrypLE Select Enzyme, 12563011, Gibco) was used as the dissociation reagent in the propagation step. Lentivirus transduction (PP7 Cherry, Plasmid #61763, Addgene) was carried out to make the cells fluorescent and resistant to the antibiotic puromycin. After the transduction, puromycin was used to kill the cells that were not transduced.

PEDOT:PSS film preparation: the electrode ink and the interconnect ink were applied to a 12-well plate and were dried in ambient to form polymer films at the bottom of the wells. The polymer films were soaked and washed three times with PBS/Anti-Anti, during which the 12-well plates were stored in a 4°C fridge. The 12-well plate was then placed in an incubator with DMEM/FBS for 3 days to test if the film was sterile. Before seeding the cells on the polymer films, they were washed three times with PBS/Anti-Anti (antibiotic-antimycotic [100×], 15240062, Gibco).

Seeding the cells: 50,000 of the transduced cells were added to each well of the 12-well plate with the PEDOT:PSS film substrate. A microscope (LSM 880, Zeiss) was used to acquire images of the cells (Figures S28 and S29). Cells directly cultured on a 12-well plate without adding any ink materials were used as a control. ImageJ software was used to outline the cells and calculate the percentage area of the cells in the entire field of view. For each sample, 2–3 fluorescent micrographs were analyzed. Because in all the experiments the cell seeding density and the field of view are the same, the percentage area can be used to reflect biocompatibility on various substrates.

### Mechanical durability and removal of the on-skin-printed e-tattoo

The ink was printed on the forearm of a subject. The dried ink was subjected to mechanical torture, such as rubbing and twisting by human hands. Then, it was removed by wiping it with an alcohol wipe or soapy water.

### Printer

A pneumatically actuated microjet tool (MDS 1560, VERMES Microdispensing GmbH) was used for non-contact ink dispensing using a 150-μm diameter nozzle at a frequency of six pulses per second, actuator pressure of 2.7 bars, and cartridge pressure of 1.7 bars. The microjet tool was integrated into a 5-axis robot system (5XM600, 5AXISWOKS LTD). The microjet dispensing and 5-axis motion (two rotational and three translational axes) were controlled via motion control software (Mach4, Newfangled Solutions) and programmed in G-code. The end-effector translation speed was capped at 200 mm/min. A custom G-code command was assigned to actuate a 24 V relay that signals the microjet controller (MDC 1500, VERMES Microdispensing GmbH) to initiate and end jetting. The 3D scanning of the scalp shape and neck used a commercial application (ScandyPro, Scandy) and was carried out by attaching a camera (iPhone 13, Apple Inc.) to the printer end effector and revolving 360° around the subject. During the scanning, the subjects used a tight-fitted elastic black cap with white cross-line patterns to aid with point tracking. This cap also compresses the hair against the scalp to assist in probing the correct scalp shape. Three holes in the cap were used to mark three fiducials on the subject's head

with a non-permanent maker (surgical skin marking pen, BrainVision LLC.). These three fiducial markers serve to match the digital head model with the physical head position. During scanning and printing, the subject sits on an adjustable massage chair with the face resting on the face pillow (Ergo Pro II, Stronglite). A 3D scan of the face is generated separately and merged with the 3D scalp scan using MeshLab to enable extracting the four reference point coordinates (nasion, inion, and left and right preauricular points) used in the 10–20 international standard for EEG placement.[4]

### EEG recording

We enrolled a total of five healthy individuals (male, aged 25–45 years). Each participant carefully reviewed and signed the informed consent form, which had been approved by the University of Texas at Austin IRB (IRB number: STUDY00002937). Consent was obtained for the publication of the images of the participants. All EEG recordings were carried out with a 32-channel EEG amplifier (LiveAmp, BrainVision) as the data acquisition system and were filtered using a bandpass filter with a range of 1–40 Hz. The experiment consists of EEG recording using conventional wet-gel electrodes and the on-scalp printed EEG system. For wet-gel electrodes, commercial EEG caps were used with Ag/AgCl electrodes (Multitrodes, EasyCap) and commercial saline gel (Signa gel, ParkerLabs).

#### *Skin preparation*

The hair was washed with shampoo and water and then allowed to dry. The electrode locations were then cleaned using an alcohol gel wipe. Throughout all experiments, the skin was not abraded in any way.

#### *Terminal connections*

First, a skin-safe glue (Spirit Gum, Mehron Makeup) is applied to the terminal locations and left for a few minutes until tacky. The 1.5-mm touch-proof carbon fiber connectors (AUVON TENS) were then placed over the glue, and a trace of interconnect ink was manually deposited to bridge the printed traces with the carbon fiber terminals. This ensured a secure and reliable electrical connection between the tattoo-like printed interconnects and the terminal connector.

#### *Electrode impedance measurements*

All five subjects participated in the impedance measurements using the commercial wet-gel and on-scalp printed electrodes. The standard 10–5 system[82] was used for the placement of 10 electrodes (Figure S25). The same five subjects, number of electrodes, and EEG amplifier were used for both electrode types (i.e., manually applied commercial wet gel and on-scalp printed e-tattoo). The impedance was measured by the amplifier connected to the neck terminal at the standard frequency of 15 Hz. The impedance was measured twice, one at 0 h and another after 6 h of electrode placement. For wet-gel recordings, an EEG cap was used, and the recording was conducted immediately after applying the wet gel. For printed electrodes, the recordings were taken after the prints had fully dried on the scalp.

#### *Motion artifact*

For the motion artifact test, the subjects were instructed to carry out the following sequential movements: "head up," "head down," "head left," "head right," "swallow," and "jaw clench," while the electrical signals were recorded by the amplifier connected to the neck terminal. We analyzed the recordings of two channels (C3 and C4) during these movements (Figure S24). Additionally, the subjects were instructed to sit and walk, and the root mean square of the recordings was calculated (Figure 4E).

#### *Interconnect insulation validation*

A custom print was carried out on the freshly washed scalp (no abrasion) of one subject using the following configuration: only the interconnect is printed for C5 and P3; both interconnects and electrodes are printed for FCC1h, FCC2h, Cz, Pz, P4, C4, and C6. For FCC2h, a thick layer of electrically insulating material (Liquid Latex, Mehron) was manually applied to the skin along the interconnect routing path before printing the interconnect ink on top. The impedance and EEG signals were measured by the amplifier (LiveAmp, BrainVision) connected to the neck terminal (Figures S22 and S23). 1-min length (3,000 samples per channel) of alpha-bandpass (8–12 Hz) filtered signals during sessions of eyes open and closed were analyzed using mutual information analysis to quantify the relationship between a pair of electrodes. High MI values can indicate a higher level of shared information between the channels, whereas low values indicate greater independence.

### BCI recording

During all the experimental sessions, we captured neural activity at eight locations in the 10–5 system[82] plus the reference and ground electrode near the mastoids. The choice of electrode positions was based on the prominent regions associated with neural markers related to two validated BCI modalities: MI[83] and error-related potential (ErrP)[67]. The positions for the on-scalp printed electrodes were CP3, C3, FC3, Cz, FCC2h, FC4, C4, and CP4. FCC2h was used instead of FCz for easier interconnect routing using our design algorithm (Note S6). P7 and P8 were the reference and the ground. For the gel electrodes, the closest available positions were selected from a cap with standard built-in electrodes (32ch BrainProducts EasyCap), which were FC5, C3, CP5, Cz, FCz, FC6, C4, and CP5. TP9 and TP10 served as the ground and reference. Figure S25 shows the montage schematic and photos of both setups.

#### *Motor imagery*

*Experimental protocol*. During the experiment, participants were instructed to either mentally imagine flexing their right hand (RH-MI class) without actually performing any physical movement or to remain in a resting state and avoid any specific thoughts (rest class). We employed a standard bar feedback-based offline session paradigm[84] to acquire the MI signals. Each session, whether using printed or gel electrodes, consisted of multiple runs. In each run, the participants performed 10 trials, with each trial belonging to either the RH-MI class or the rest class. The order of the trials was randomized. The trials followed a specific sequence. First, a fixation cross was presented for 2 s, during which the participants were instructed to prepare for the upcoming cue. This was followed by the presentation of a cue (either rest or RH-MI) for 1.5 s. After the cue presentation, the participants were presented with visual feedback in the form of a moving bar or circle. The feedback was displayed for 5 s and guided the participants based on the targeted cue. Specifically, a moving bar or circle appeared on the corresponding side of the targeted cue (Figure 5A). The circle represented the resting state, whereas the rectangle represented the RH-MI class. The trial concluded with a 2-s presentation of the trial result, followed by a 1.5-s inter-trial rest period before the start of the next trial.

*Motor imagery characterization*. We used state-of-the-art minimum distance to mean (MDM) Riemannian geometry classifier (RGC) for motor imagery decoding.[65,85] RGC uses covariance matrices of bandpass-filtered multi-channel EEG data as features for MI signal classification. In brevity, positive definite covariance matrices reside on the Riemannian manifold, which can be embedded using the affine invariant Riemannian metric (AIRM). The AIRM allows for defining the concept of Riemannian distance on the manifold, which is utilized in training the MDM classifiers. Refer to Yger et al.[86] for a detailed description.

To obtain an unbiased estimation of the classification performance, we employed a leave-one-run-out cross-validation (LOROCV) strategy. This involved using all runs except one as training data to build the classifier and then evaluating the performance on the left-out run. This process was iterated for each run, and the average classification performance across all runs was reported. After recording the signals, we visually inspected all the channels and rejected the EEG data from channels that appeared as flatlines or recorded exceptionally high amplitudes. For LOROCV analysis, we bandpassed the signals in [8–30] Hz and used 1-s samples with 0.05-s step size. In all MI-BCI analyses, we further discarded samples in which any data point within the 1-s segment exceeded an absolute value of 100 $\mu$V. To characterize the signal quality, we estimated the fraction of samples out of total of 1-s samples during the task period that were not rejected according to the earlier mentioned rejection criteria.

For the ERD analysis, we calculated the baseline power ($p_{c,t}^{rest}$) using a 1-s window from the fixation period. Subsequently, the task power ($p_{c,t}^{task}$) was estimated using non-overlapping 1-s windows beginning 0.5 s after the presentation of the cue. We excluded the initial 0.5-s period after the task presentation to avoid the influence of visually evoked potentials. We then estimated the ERD value for a trial $t$ of $c^{th}$ channel as

$$ERD_{c,t} = \frac{p_{c,t}^{rest} - \underset{n \in (1,5)}{\operatorname{argmin}}\, p_{c,t}^{task}}{p_{c,t}^{rest}} \quad \text{(Equation 2)}$$

where n is the number of non-overlapping windows during the task period (in our current experiment, n ranges from 1 to 5).

### *ErrP*

To test whether our proposed system could be used for ErrP detection, we collected 8-channel EEG data from four runs of visual ErrP tasks in five subjects. In these tasks, the subjects were instructed to monitor the cursor movement and evaluate if the cursor moved toward a target position (marked in red) correctly or erroneously. The subject had no control over the cursor movements, and the cursor moved horizontally every 2,000 to 2,500 ms across a 1D space composed of 10 positions (Figure 5A). The cursor moved away from the target with a 30% chance of the trials. When the cursor reached the target position, a new target location was chosen randomly.

We performed event-related potential (ERP) and classification analysis on ErrP data following these steps. EEG data from four blocks for individual subjects were concatenated and bandpass filtered between 1 to 10 Hz using a non-causal fourth-order Butterworth filter. Time samples from the time window (−1.3 s before to until 1.5 s after stimulus onset) were chosen and segmented as epochs. Baseline correction was applied using the 100 ms window prior to stimulus onset. Trials that contained time points above the absolute value of 50 μV in any channel were rejected from epochs. ERP analysis was performed by averaging all of the epochs from all subjects with respect to error and correct conditions. In the classification analysis, we used the window [0.2, 0.8] s after the onset of the cursor movement, downsampled to 64 Hz. Features corresponded to the EEG voltage of each time sample and the power spectral density (PSD) between 1–10 Hz from all eight channels. Features were min-max normalized to values between 0 and 1. The classification accuracy was computed using leave-one-run-out run-wise cross-validation from the four blocks, using diagonal linear discriminant analysis (LDA).

## RESOURCE AVAILABILITY

### Lead contact

Further information and requests for resources and reagents should be directed to and will be fulfilled by the lead contact, Nanshu Lu (nanshulu@utexas.edu).

### Material availability

This study did not generate new, unique materials.

### Data and code availability

The authors declare that the data supporting the findings of this study are available within the article and its supplemental information files as well as from the corresponding author upon reasonable request. The algorithm for custom electrode-interconnect layout design and G-code generation is available at: https://doi.org/10.5281/zenodo.14015242.

## ACKNOWLEDGMENTS

N.L. acknowledges the support from the US Army Research Office under Cooperative Agreement W911NF-19-2-0333. The views and conclusions contained in this article are those of the authors and should not be interpreted as representing the official policies, either expressed or implied, of the US Army Research Office or the US government. X.M. and M.G.M. acknowledge the support of the National Institutes of Health (NIH) R01 award DK132319-02, American Society of Chemistry Petroleum Research Funding PRF# 66747-ND7, and the Johnson & Johnson WISTEM2D Scholars Program Award. J.d.R.M. acknowledges support from the Coleman Fung Foundation.

## AUTHOR CONTRIBUTIONS

N.L. designed the research. L.S.d.V., N.L., E.W., and C.B. conceived and implemented the 5-axis on-scalp microjetting platform. S.T., E.L., and L.S.d.V. wrote the electrode-interconnect design and printer control algorithms. H.L. and P.V. carried out ink breathability experiments, interconnect insulation validation study, and film conformability cross-section measurements on porcine skin. Y.Y., B.Y., X.H., L.S.d.V., and N.L. carried out the ink development. W.H. carried out sweat stability and contact angle measurements. Z.L. carried out the mechanical analysis of skin conformability using the energy minimization method. Y.Y., B.Y., L.S.d.V., P.M., S.D., and E.W. characterized the electrical and mechanical properties of the interconnect and electrode inks. Y.Y., Y.D., R.S.S.-V., and M.G.M. characterized cell biocompatibility. S.K., M.Z., F.I., and J.d.R.M. designed the BCI experiments. P.M., M.Z., S.K., E.L., A.T.R., P.T., and P.W. carried out BCI experiments, including human subject preparation, head scanning, printing, and analysis. L.S.d.V., Y.Y., S.K. M.Z., H.L., P.M., S.D., Z.L., P.V., P.T.T., J.d.R.M., X.H., and N.L. wrote the paper.

## DECLARATION OF INTERESTS

N.L. is on the advisory board of *Cell Biomaterials*. J.d.R.M. is a consultant for Meta Reality Labs Research.

## DECLARATION OF GENERATIVE AI AND AI-ASSISTED TECHNOLOGIES IN THE WRITING PROCESS

During the preparation of this manuscript, the authors used TexGPT only to polish the language. After using this tool, the authors reviewed and edited the content as needed and take full responsibility for the content of the publication.

## SUPPLEMENTAL INFORMATION

Supplemental information can be found online at https://doi.org/10.1016/j.celbio.2024.100004.

Received: September 16, 2024
Revised: October 25, 2024
Accepted: November 1, 2024
Published: December 2, 2024

## REFERENCES

1. Michel, C.M., Murray, M.M., Lantz, G., Gonzalez, S., Spinelli, L., and Grave de Peralta, R.G. (2004). EEG source imaging. Clin. Neurophysiol. *115*, 2195–2222. https://doi.org/10.1016/j.clinph.2004.06.001.
2. Niedermeyer, E., and da Silva, F.L. (2005). Electroencephalography: Basic Principles, Clinical Applications, and Related Fields (Lippincott Williams & Wilkins).
3. Ramsey, N.F. (2020). Human brain function and Brain-Computer Interfaces. Handb. Clin. Neurol. *168*, 1–13. https://doi.org/10.1016/B978-0-444-63934-9.00001-9.
4. Jasper, H. (1958). Report of the committee on methods of clinical examination in electroencephalography. Electroencephalogr. Clin. Neurophysiol. *10*, 370–375. https://doi.org/10.1016/0013-4694(58)90053-1.
5. Kolls, B.J., Lai, A.H., Srinivas, A.A., and Reid, R.R. (2014). Integration of EEG lead placement templates into traditional technologist-based staffing models reduces costs in continuous video-EEG monitoring service. J. Clin. Neurophysiol. *31*, 187–193. https://doi.org/10.1097/WNP.0000000000000053.
6. Kolls, B.J., Olson, D.M., Gallentine, W.B., Skeen, M.B., Skidmore, C.T., and Sinha, S.R. (2012). Electroencephalography leads placed by nontechnologists using a template system produce signals equal in quality to technologist-applied, collodion disk leads. J. Clin. Neurophysiol. *29*, 42–49. https://doi.org/10.1097/WNP.0b013e318246ae76.
7. Beam, W., Borckardt, J.J., Reeves, S.T., and George, M.S. (2009). An efficient and accurate new method for locating the f3 position for prefrontal tms applications. Brain Stimul. *2*, 50–54. https://doi.org/10.1016/j.brs.2008.09.006.
8. Li, J., Ma, Y., Huang, D., Wang, Z., Zhang, Z., Ren, Y., Hong, M., Chen, Y., Li, T., Shi, X., et al. (2022). High-performance flexible microneedle array as a low-impedance surface biopotential dry electrode for wearable electrophysiological recording and polysomnography. Nano Micro Lett. *14*, 132. https://doi.org/10.1007/s40820-022-00870-0.

9. Kennedy, J.D., and Gerard, E.E. (2012). Continuous EEG monitoring in the intensive care unit. Curr. Neurol. Neurosci. Rep. *12*, 419–428. https://doi.org/10.1007/s11910-012-0289-0.

10. Falco, C., Sebastiano, F., Cacciola, L., Orabona, F., Ponticelli, R., Stirpe, P., and Di Gennaro, G. (2005). Scalp electrode placement by EC2® adhesive paste in long-term video-EEG monitoring. Clin. Neurophysiol. *116*, 1771–1773. https://doi.org/10.1016/j.clinph.2005.04.012.

11. Kim, D.-H., Lu, N., Ma, R., Kim, Y.-S., Kim, R.-H., Wang, S., Wu, J., Won, S.M., Tao, H., Islam, A., et al. (2011). Epidermal electronics. Science *333*, 838–843. https://doi.org/10.1126/science.1206157.

12. Li, H., Tan, P., Rao, Y., Bhattacharya, S., Wang, Z., Kim, S., Gangopadhyay, S., Shi, H., Jankovic, M., Huh, H., et al. (2024). E-tattoos: Toward functional but imperceptible interfacing with human skin. Chem. Rev. *124*, 3220–3283. https://doi.org/10.1021/acs.chemrev.3c00626.

13. Ray, T.R., Choi, J., Bandodkar, A.J., Krishnan, S., Gutruf, P., Tian, L., Ghaffari, R., and Rogers, J.A. (2019). Bio-integrated wearable systems: a comprehensive review. Chem. Rev. *119*, 5461–5533. https://doi.org/10.1021/acs.chemrev.8b00573.

14. Sunwoo, S.-H., Ha, K.-H., Lee, S., Lu, N., and Kim, D.-H. (2021). Wearable and implantable soft bioelectronics: device designs and material strategies. Annu. Rev. Chem. Biomol. Eng. *12*, 359–391. https://doi.org/10.1146/annurev-chembioeng-101420-024336.

15. Liu, S., Rao, Y., Jang, H., Tan, P., and Lu, N. (2022). Strategies for body-conformable electronics. Matter *5*, 1104–1136. https://doi.org/10.1016/j.matt.2022.02.006.

16. Luo, Y., Abidian, M.R., Ahn, J.-H., Akinwande, D., Andrews, A.M., Antonietti, M., Bao, Z., Berggren, M., Berkey, C.A., Bettinger, C.J., et al. (2023). Technology roadmap for flexible sensors. ACS Nano *17*, 5211–5295. https://doi.org/10.1021/acsnano.2c12606.

17. Tan, P., Tamma, S., Bhattacharya, S., Tunnell, J., and Lu, N. (2022). Wearable optical e-tattoo for deep neck hemodynamic monitoring. In 2022 IEEE/ACM Conference on Connected Health: Applications, Systems and Engineering Technologies (CHASE), pp. 118–122. https://doi.org/10.1145/3551455.3559604.

18. García-López, I., and Rodriguez-Villegas, E. (2020). Extracting the jugular venous pulse from anterior neck contact photoplethysmography. Sci. Rep. *10*, 3466. https://doi.org/10.1038/s41598-020-60317-7.

19. Zipp, P. (1982). Recommendations for the standardization of lead positions in surface electromyography. Eur. J. Appl. Physiol. Occup. Physiol. *50*, 41–54. https://doi.org/10.1007/BF00952243.

20. Ratti, E., Waninger, S., Berka, C., Ruffini, G., and Verma, A. (2017). Comparison of medical and consumer wireless EEG systems for use in clinical trials. Front. Hum. Neurosci. *11*, 398. https://doi.org/10.3389/fnhum.2017.00398.

21. Yin, J., Wang, S., Tat, T., and Chen, J. (2024). Motion artefact management for soft bioelectronics. Nat. Rev. Bioeng. *2*, 541–558. https://doi.org/10.1038/s44222-024-00175-4.

22. Tian, L., Zimmerman, B., Akhtar, A., Yu, K.J., Moore, M., Wu, J., Larsen, R.J., Lee, J.W., Li, J., Liu, Y., et al. (2019). Large-area mri-compatible epidermal electronic interfaces for prosthetic control and cognitive monitoring. Nat. Biomed. Eng. *3*, 194–205. https://doi.org/10.1038/s41551-019-0347-x.

23. Hure, J., Roman, B., and Bico, J. (2011). Wrapping an adhesive sphere with an elastic sheet. Phys. Rev. Lett. *106*, 174301. https://doi.org/10.1103/PhysRevLett.106.174301.

24. Liu, S., He, J., Rao, Y., Dai, Z., Ye, H., Tanir, J.C., Li, Y., and Lu, N. (2023). Conformability of flexible sheets on spherical surfaces. Sci. Adv. *9*, eadf2709. https://doi.org/10.1126/sciadv.adf2709.

25. Wang, Y., Yin, L., Bai, Y., Liu, S., Wang, L., Zhou, Y., Hou, C., Yang, Z., Wu, H., Ma, J., et al. (2020). Electrically compensated, tattoo-like electrodes for epidermal electrophysiology at scale. Sci. Adv. *6*, 0996. https://doi.org/10.1126/sciadv.abd0996.

26. Ershad, F., Houston, M., Patel, S., Contreras, L., Koirala, B., Lu, Y., Rao, Z., Liu, Y., Dias, N., Haces-Garcia, A., et al. (2023). Customizable, reconfigurable, and anatomically coordinated large-area, high-density electromyography from drawn-on-skin electrode arrays. PNAS Nexus *2*, pgac291. https://doi.org/10.1093/pnasnexus/pgac291.

27. Kayser, L.V., and Lipomi, D.J. (2019). Stretchable conductive polymers and composites based on pedot and pedot:pss. Adv. Mater. *31*, e1806133. https://doi.org/10.1002/adma.201806133.

28. He, H., Zhang, L., Guan, X., Cheng, H., Liu, X., Yu, S., Wei, J., and Ouyang, J. (2019). Biocompatible conductive polymers with high conductivity and high stretchability. ACS Appl. Mater. Interfaces *11*, 26185–26193. https://doi.org/10.1021/acsami.9b07325.

29. Zhang, L., Kumar, K.S., He, H., Cai, C.J., He, X., Gao, H., Yue, S., Li, C., Seet, R.C.S., Ren, H., and Ouyang, J. (2020). Fully organic compliant dry electrodes self-adhesive to skin for long-term motion-robust epidermal biopotential monitoring. Nat. Commun. *11*, 4683. https://doi.org/10.1038/s41467-020-18503-8.

30. Zhang, S., Chen, Y., Liu, H., Wang, Z., Ling, H., Wang, C., Ni, J., Çelebi-Saltik, B., Wang, X., Meng, X., et al. (2020). Room-temperature-formed pedot:pss hydrogels enable injectable, soft, and healable organic bioelectronics. Adv. Mater. *32*, e1904752. https://doi.org/10.1002/adma.201904752.

31. Zhu, Z., Guo, S.-Z., Hirdler, T., Eide, C., Fan, X., Tolar, J., and McAlpine, M.C. (2018). 3D printed functional and biological materials on moving free-form surfaces. Adv. Mater. *30*, e1707495. https://doi.org/10.1002/adma.201707495.

32. Zhao, W., Chen, H., Zhang, Y., Zhou, D., Liang, L., Liu, B., and Xu, T. (2022). Adaptive multi-degree-of-freedom in situ bioprinting robot for hair-follicle-inclusive skin repair: A preliminary study conducted in mice. Bioeng. Transl. Med. *7*, e10303. https://doi.org/10.1002/btm2.10303.

33. Kucukdeger, E., and Johnson, B.N. (2023). Closed-loop controlled conformal 3D printing on moving objects via tool-localized object position sensing. J. Manuf. Process *89*, 39–49. https://doi.org/10.1016/j.jmapro.2023.01.020.

34. Choi, Y., Ryu, N., Kim, M.J., Dementyev, A., and Bianchi, A. (2020). Bodyprinter: Fabricating circuits directly on the skin at arbitrary locations using a wearable compact plotter. In Proceedings of the 33rd Annual ACM Symposium on User Interface Software and Technology, pp. 554–564. https://doi.org/10.1145/3379337.3415840.

35. Zhu, Z., Park, H.S., and McAlpine, M.C. (2020). 3D printed deformable sensors. Sci. Adv. *6*, eaba5575. https://doi.org/10.1126/sciadv.aba5575.

36. Park, J.-U., Hardy, M., Kang, S.J., Barton, K., Adair, K., Mukhopadhyay, D.K., Lee, C.Y., Strano, M.S., Alleyne, A.G., Georgiadis, J.G., et al. (2007). High-resolution electrohydrodynamic jet printing. Nat. Mater. *6*, 782–789. https://doi.org/10.1038/nmat1974.

37. Lin, L., Dautta, M., Hajiaghajani, A., Escobar, A.R., Tseng, P., and Khine, M. (2021). Paint-on epidermal electronics for on-demand sensors and circuits. Adv. Electron. Mater. *7*, 2000765. https://doi.org/10.1002/aelm.202000765.

38. Williams, N.X., Noyce, S., Cardenas, J.A., Catenacci, M., Wiley, B.J., and Franklin, A.D. (2019). Silver nanowire inks for direct-write electronic tattoo applications. Nanoscale *11*, 14294–14302. https://doi.org/10.1039/C9NR03378E.

39. Zhang, L., Ji, H., Huang, H., Yi, N., Shi, X., Xie, S., Li, Y., Ye, Z., Feng, P., Lin, T., et al. (2020). Wearable circuits sintered at room temperature directly on the skin surface for health monitoring. ACS Appl. Mater. Interfaces *12*, 45504–45515. https://doi.org/10.1021/acsami.0c11479.

40. Ershad, F., Thukral, A., Yue, J., Comeaux, P., Lu, Y., Shim, H., Sim, K., Kim, N.-I., Rao, Z., Guevara, R., et al. (2020). Ultra-conformal drawn-on-skin electronics for multifunctional motion artifact-free sensing and point-of-care treatment. Nat. Commun. *11*, 3823. https://doi.org/10.1038/s41467-020-17619-1.

41. Falland-Cheung, L., Scholze, M., Lozano, P.F., Ondruschka, B., Tong, D.C., Brunton, P.A., Waddell, J.N., and Hammer, N. (2018). Mechanical properties of the human scalp in tension. J. Mech. Behav. Biomed. Mater. *84*, 188–197. https://doi.org/10.1016/j.jmbbm.2018.05.024.

42. Huang, Q., and Zheng, Z. (2022). Pathway to developing permeable electronics. ACS Nano *16*, 15537–15544. https://doi.org/10.1021/acsnano.2c08091.

43. Ferree, T.C., Luu, P., Russell, G.S., and Tucker, D.M. (2001). Scalp electrode impedance, infection risk, and EEG data quality. Clin. Neurophysiol. *112*, 536–544. https://doi.org/10.1016/S1388-2457(00)00533-2.

44. Mantione, D., Del Agua, I., Sanchez-Sanchez, A., and Mecerreyes, D. (2017). Poly(3,4-ethylenedioxythiophene) (pedot) derivatives: Innovative conductive polymers for bioelectronics. Polymers *9*, 354. https://doi.org/10.3390/polym9080354.

45. Yuk, H., Lu, B., Lin, S., Qu, K., Xu, J., Luo, J., and Zhao, X. (2020). 3D printing of conducting polymers. Nat. Commun. *11*, 1604. https://doi.org/10.1038/s41467-020-15316-7.

46. Liu, Y., Liu, J., Chen, S., Lei, T., Kim, Y., Niu, S., Wang, H., Wang, X., Foudeh, A.M., Tok, J.B.-H., and Bao, Z. (2019). Soft and elastic hydrogel-based microelectronics for localized low-voltage neuromodulation. Nat. Biomed. Eng. *3*, 58–68. https://doi.org/10.1038/s41551-018-0335-6.

47. Murray, K.A., and Gibson, M.I. (2022). Chemical approaches to cryopreservation. Nat. Rev. Chem. *6*, 579–593. https://doi.org/10.1038/s41570-022-00407-4.

48. Lu, B., Yuk, H., Lin, S., Jian, N., Qu, K., Xu, J., and Zhao, X. (2019). Pure pedot:pss hydrogels. Nat. Commun. *10*, 1043. https://doi.org/10.1038/s41467-019-09003-5.

49. Fluhr, J.W., Darlenski, R., and Surber, C. (2008). Glycerol and the skin: holistic approach to its origin and functions. Br. J. Dermatol. *159*, 23–34. https://doi.org/10.1111/j.1365-2133.2008.08643.x.

50. Liu, Y., Li, J., Song, S., Kang, J., Tsao, Y., Chen, S., Mottini, V., McConnell, K., Xu, W., Zheng, Y.-Q., et al. (2020). Morphing electronics enable neuromodulation in growing tissue. Nat. Biotechnol. *38*, 1031–1036. https://doi.org/10.1038/s41587-020-0495-2.

51. Shi, H., Liu, C., Jiang, Q., and Xu, J. (2015). Effective approaches to improve the electrical conductivity of pedot:pss: A review. Adv. Electron. Mater. *1*, 1500017. https://doi.org/10.1002/aelm.201500017.

52. Ma, Z., Huang, Q., Xu, Q., Zhuang, Q., Zhao, X., Yang, Y., Qiu, H., Yang, Z., Wang, C., Chai, Y., and Zheng, Z. (2021). Permeable superelastic liquid-metal fibre mat enables biocompatible and monolithic stretchable electronics. Nat. Mater. *20*, 859–868. https://doi.org/10.1038/s41563-020-00902-3.

53. Yoon, S., Seok, M., Kim, M., and Cho, Y.-H. (2021). Wearable porous pdms layer of high moisture permeability for skin trouble reduction. Sci. Rep. *11*, 938. https://doi.org/10.1038/s41598-020-78580-z.

54. Webster, J.G. (2006). Encyclopedia of Medical Devices and Instrumentation (John Wiley & Sons, Inc.).

55. He, H., Chen, R., Yue, S., Yu, S., Wei, J., and Ouyang, J. (2022). Salt-induced ductilization and strain-insensitive resistance of an intrinsically conducting polymer. Sci. Adv. *8*, eabq8160. https://doi.org/10.1126/sciadv.abq8160.

56. Jung, S., and Hutchings, I.M. (2012). The impact and spreading of a small liquid drop on a non-porous substrate over an extended time scale. Soft Matter *8*, 2686–2696. https://doi.org/10.1039/C2SM06565G.

57. Bießmann, L., Kreuzer, L.P., Widmann, T., Hohn, N., Moulin, J.-F., and Müller-Buschbaum, P. (2018). Monitoring the Swelling Behavior of PEDOT:PSS Electrodes under High Humidity Conditions. ACS Appl. Mater. Interfaces *10*, 9865–9872. https://doi.org/10.1021/acsami.8b00446.

58. Dalal, S.S., Rampp, S., Willomitzer, F., and Ettl, S. (2014). Consequences of EEG electrode position error on ultimate beamformer source reconstruction performance. Front. Neurosci. *8*, 80684. https://doi.org/10.3389/fnins.2014.00042.

59. Giacometti, P., Perdue, K.L., and Diamond, S.G. (2014). Algorithm to find high density EEG scalp coordinates and analysis of their correspondence to structural and functional regions of the brain. J. Neurosci. Methods *229*, 84–96. https://doi.org/10.1016/j.jneumeth.2014.04.020.

60. Herman, S.T., Abend, N.S., Bleck, T.P., Chapman, K.E., Drislane, F.W., Emerson, R.G., Gerard, E.E., Hahn, C.D., Husain, A.M., Kaplan, P.W., et al. (2015). Consensus statement on continuous EEG in critically ill adults and children, part ii: personnel, technical specifications, and clinical practice. J. Clin. Neurophysiol. *32*, 96–108. https://doi.org/10.1097/WNP.0000000000000165.

61. Dai, H., Pears, N., Smith, W., and Duncan, C. (2020). Statistical modeling of craniofacial shape and texture. Int. J. Comput. Vision *128*, 547–571. https://doi.org/10.1007/s11263-019-01260-7.

62. Park, B.D., Corner, B.D., Hudson, J.A., Whitestone, J., Mullenger, C.R., and Reed, M.P. (2021). A three-dimensional parametric adult head model with representation of scalp shape variability under hair. Appl. Ergon. *90*, 103239. https://doi.org/10.1016/j.apergo.2020.103239.

63. Burbank, D.P., and Webster, J.G. (1978). Reducing skin potential motion artefact by skin abrasion. Med. Biol. Eng. Comput. *16*, 31–38. https://doi.org/10.1007/BF02442929.

64. Kappenman, E.S., and Luck, S.J. (2010). The effects of electrode impedance on data quality and statistical significance in erp recordings. Psychophysiology *47*, 888–904. https://doi.org/10.1111/j.1469-8986.2010.01009.x.

65. Kumar, S., Alawieh, H., Racz, F.S., Fakhreddine, R., and Millán, J.D.R. (2024). Transfer learning promotes acquisition of individual BCI skills. PNAS Nexus *3*, pgae076. https://doi.org/10.1093/pnasnexus/pgae076.

66. Alawieh, H., Liu, D., Madera, J., Kumar, S., Racz, F.S., Majewicz Fey, A., and Millán, J.d.R. (2024). Transcutaneous electrical spinal cord stimulation promotes focal sensorimotor activation that accelerates brain-computer interface skill learning. Preprint at medRxiv.

67. Chavarriaga, R., Sobolewski, A., and Millán, J.d.R. (2014). Errare machinale est: the use of error-related potentials in brain-machine interfaces. Front. Neurosci. *8*, 86996. https://doi.org/10.3389/fnins.2014.00208.

68. Iwane, F., Iturrate, I., Chavarriaga, R., and Millán, J.D.R. (2021). Invariability of EEG error-related potentials during continuous feedback protocols elicited by erroneous actions at predicted or unpredicted states. J. Neural Eng. *18*, 888046044. https://doi.org/10.1088/1741-2552/abfa70.

69. Choy, T., Baker, E., and Stavropoulos, K. (2022). Systemic racism in EEG research: considerations and potential solutions. Affect. Sci. *3*, 14–20. https://doi.org/10.1007/s42761-021-00050-0.

70. Webb, E.K., Etter, J.A., and Kwasa, J.A. (2022). Addressing racial and phenotypic bias in human neuroscience methods. Nat. Neurosci. *25*, 410–414. https://doi.org/10.1038/s41593-022-01046-0.

71. Etienne, A., Laroia, T., Weigle, H., Afelin, A., Kelly, S.K., Krishnan, A., and Grover, P. (2020). Novel electrodes for reliable EEG recordings on coarse and curly hair. In Annu. Int. Conf. IEEE Eng. Med. Biol. Soc. 42nd Annual International Conference of the IEEE Engineering in Medicine & Biology Society (EMBC) (IEEE Publications), pp. 6151–6154. https://doi.org/10.1109/EMBC44109.2020.9176067.

72. Li, H., Shin, H., Sentis, L., Siu, K.-C., Millán, J.d.R., and Lu, N. (2024). Combining VRhigh with electroencephalography as a frontier of brain-computer interfaces. Device *2*, 100425. https://doi.org/10.1016/j.device.2024.100425.

73. Park, Y.-G., Yun, I., Chung, W.G., Park, W., Lee, D.H., and Park, J.-U. (2022). High-resolution 3D printing for electronics. Adv. *9*, e2104623. https://doi.org/10.1002/advs.202104623.

74. Park, Y.-G., Kwon, Y.W., Koh, C.S., Kim, E., Lee, D.H., Kim, S., Mun, J., Hong, Y.-M., Lee, S., Kim, J.-Y., et al. (2024). In-vivo integration of soft neural probes through high-resolution printing of liquid electronics on the cranium. Nat. Commun. *15*, 1772. https://doi.org/10.1038/s41467-024-45768-0.

75. Li, N., Li, Y., Cheng, Z., Liu, Y., Dai, Y., Kang, S., Li, S., Shan, N., Wai, S., Ziaja, A., et al. (2023). Bioadhesive polymer semiconductors and

transistors for intimate biointerfaces. Science *381*, 686–693. https://doi.org/10.1126/science.adg8758.

76. Cao, Y., Tan, J., Zhao, H., Deng, T., Hu, Y., Zeng, J., Li, J., Cheng, Y., Tang, J., Hu, Z., et al. (2022). Bead-jet printing enabled sparse mesenchymal stem cell patterning augments skeletal muscle and hair follicle regeneration. Nat. Commun. *13*, 7463. https://doi.org/10.1038/s41467-022-35183-8.

77. Li, L., Yu, F., Shi, J., Shen, S., Teng, H., Yang, J., Wang, X., and Jiang, Q. (2017). In situ repair of bone and cartilage defects using 3D scanning and 3D printing. Sci. Rep. *7*, 9416. https://doi.org/10.1038/s41598-017-10060-3.

78. Kérourédan, O., Hakobyan, D., Rémy, M., Ziane, S., Dusserre, N., Fricain, J.-C., Delmond, S., Thébaud, N.B., and Devillard, R. (2019). In situ prevascularization designed by laser-assisted bioprinting: effect on bone regeneration. Biofabrication *11*, 045002. https://doi.org/10.1088/1758-5090/ab2620.

79. Barone, D.G., and Malliaras, G.G. (2019). Epidermal electrophysiology at scale. Nat. Biomed. Eng. *3*, 165–166. https://doi.org/10.1038/s41551-019-0365-8.

80. Kwon, Y.W., Ahn, D.B., Park, Y.-G., Kim, E., Lee, D.H., Kim, S.-W., Lee, K.-H., Kim, W.-Y., Hong, Y.-M., Koh, C.S., et al. (2024). Power-integrated, wireless neural recording systems on the cranium using a direct printing method for deep-brain analysis. Sci. Adv. *10*, eadn3784. https://doi.org/10.1126/sciadv.adn3784.

81. Wang, L., and Lu, N. (2016). Conformability of a Thin Elastic Membrane Laminated on a Soft Substrate With Slightly Wavy Surface. J. Appl. Mech. *83*, 041007. https://doi.org/10.1115/1.4032466.

82. Oostenveld, R., and Praamstra, P. (2001). The five percent electrode system for high-resolution EEG and ERP measurements. Clin. Neurophysiol. *112*, 713–719. https://doi.org/10.1016/S1388-2457(00)00527-7.

83. Perdikis, S., Tonin, L., Saeedi, S., Schneider, C., and Millán, J.D.R. (2018). The Cybathlon BCI race: Successful longitudinal mutual learning with two tetraplegic users. PLOS Biol. *16*, e2003787. https://doi.org/10.1371/journal.pbio.2003787.

84. Leeb, R., Perdikis, S., Tonin, L., Biasiucci, A., Tavella, M., Creatura, M., Molina, A., Al-Khodairy, A., Carlson, T., and Millán, J.D.R. (2013). Transferring brain-computer interfaces beyond the laboratory: Successful application control for motor-disabled users. Artif. Intell. Med. *59*, 121–132. https://doi.org/10.1016/j.artmed.2013.08.004.

85. Barachant, A., Bonnet, S., Congedo, M., and Jutten, C. (2012). Multiclass brain-computer interface classification by Riemannian geometry. IEEE Trans. Bio Med. Eng. *59*, 920–928. https://doi.org/10.1109/TBME.2011.2172210.

86. Yger, F., Berar, M., and Lotte, F. (2017). Riemannian approaches in brain-computer interfaces: A review. IEEE Trans. Neural Syst. Rehabil. Eng. *25*, 1753–1762. https://doi.org/10.1109/TNSRE.2016.2627016.